ROYAL SOCIETY OF CHEMISTRY

COMMUNICATION

Check for updates

Fabricating 3A optical films *via* transfer printing from a nickel nanocone array template†

Kun Gan,‡[a,b] Shanlin Li,‡[a] Haojie Zhu,[a] Weisheng Pan,[a] Rui Yao[a] and Cheng Yang (ID) *[a]

Nanostructured surfaces are fundamental for the development of various functional films. Nanoimprint technology enables the transfer of patterns from templates with micro−nano structures onto various substrates to achieve advanced functionalities. However, developing practical large-area periodic templates and achieving high-performance thin layers through imprinting have been challenging. This study presents a method for creating nickel nanocone arrays (NCAs) *via* electrodeposition as nanoimprint templates. By employing the nanostructured surfaces as templates to transfer-print optical resins, optical films with anti-glare (AG) functionality were fabricated. Additionally, anti-fingerprint (AF) resin with a specific thickness is coated on the surface of the optical films to achieve both anti-reflective (AR) and AF functionalities. The 3A optical films demonstrate exceptional properties, characterized by high hydrophobicity, low reflectivity, high transmittance, and desirable haze. This showcases the promising application potential of this innovative technology in the field of 3A optical films as well as in photovoltaic panel applications.

Introduction

Display panels are essential components in daily life, covering various industries including consumer electronics, education, automotive industry, healthcare, retail and advertising, manufacturing and sports and entertainment.[1] While a bare display panel can offer fundamental visual capabilities, covering a protective optical polymer film over it can enhance the viewing experience and protective functionality in complex environments. Preferentially, this film should be able to effectively reduce glare, reflections, and fingerprint smudges, ensuring a clearer and more comfortable viewing experience.

[a]*Institute of Materials Research, Tsinghua Shenzhen International Graduate School, Tsinghua, Shenzhen, 518055, China. E-mail: yang.cheng@sz.tsinghua.edu.cn*

[b]*Shenzhen Sunroll Tech. Co. Ltd, Shenzhen, 518106, China*

†Electronic supplementary information (ESI) available. See DOI: https://doi.org/10.1039/d5nr00089k

‡These authors contributed equally.

The phenomenon of "glare" (Anti-Glare, AG) arises from interference caused by ambient light, leading to discomfort due to inadequate brightness or contrast on the panel. Typically, glare is the result of strong light sources behind the viewer reflected on the screen. This issue becomes particularly pronounced in bright ambient conditions(*e.g.*, outdoors), making images harder to discern and potentially causing eye fatigue during prolonged viewing.[2] The intense diffuse reflection on the surface of displays can diminish screen blackness, resulting in a significant decline in clarity and color saturation. Therefore, it is essential to reduce surface reflectivity (anti-reflection, AR).[3] Furthermore, the screen surface is prone to contamination from skin oils, sweat, and dust, which affects both its appearance and usability. Consequently, development of optical films with anti-fingerprint (AF) properties is crucial.[4]

A 3A optical film is an optical film that simultaneously possesses the aforementioned three functionalities—AG, AR, and AF. It can serve as an ideal protective layer for displays as well as various gadgets and facilities. Regrettably, although a few commercial optical film products with 1A or 2A characteristics exist, achieving all 3A functionalities concurrently has remained a significant challenge. Incorporating microspheres with a different refractive index (*e.g.* SiO_2 micro spheres) into an optically clear polymer coating can enhance diffuse reflection, thereby achieving AG functionality (1A). To achieve AR functionality, applying multiple coating layers with gradient refractive indices reduces interference of incident and reflected light, which has been primarily accomplished through multilayer vacuum deposition (*e.g.* magneto sputtering and chemical vapor deposition). Finally, AF functionality can be realized by a thin layer of hydrophobic and oleo-phobic resin coating, such as that used in eyeglasses (2A). It is evident that developing a 3A optical film that effectively incorporates AG, AR, and AF properties involves complex technologies and multiple steps. Thus, achieving simple, scalable, and general production remains a challenging yet important task.

Applying micro−nano structures to the surface of a smooth optical film, along with selecting appropriate resins for AG, AR, and AF functionalities, are critical steps.[5] It is thus

essential to first prepare optical films with a haze level, typically between 25% and 40%, for a wide range of display panel market applications. One viable method involves pre-fabricating specific micro–nano structural patterns on a rigid template and then transferring these patterns onto an optical film to create specific regular nanopatterns. This technique, known as transfer printing or nanoimprint, allows for the efficient and precise processing of various materials into specific micro–nano structures. Its primary advantages include high resolution, high production throughput, low cost, and flexible material selection, making it promising for widespread applications in microelectronics, micro–nano fabrication, and nanotechnology.[6,7]

The basic process of nanoimprinting consists of three steps: template preparation, pattern replication, and pattern transfer.[8] Initially, a nano-pattern-etched template is brought into contact with a resin-based film precursor. Under specific curing conditions (including time, pressure, temperature, and light illumination), the resin rapidly solidifies. Subsequent separation of the template allows precise pattern replication. This transfer process can be repeated to achieve mass production of optical films with surface nanostructures.[9]

Even though the process seems simple, the preparation of templates is a challenging step, often relying on high-precision photolithography. The authors' lab has explored electrodeposition methods for constructing micro–nano array structures.[10–13] These methods allow for transferring desired nanostructures onto the surface of the optical film. Nickel nanocone arrays (NCAs), known for their excellent mechanical strength and chemical stability, can be fabricated through electrodeposition; their formation mechanism is explained by spiral dislocation-driven crystal growth theory.[10] The growth process involved in this mechanism includes the generation of step edges by spiral dislocations, thereby accelerating crystal growth along the dislocation center V_c direction. The growth occurs in a self-sustaining spiral manner along the dislocation. Depending on the nature of the spiral dislocation, there are two distinct growth directions in electrodeposition: one along the direction of V_c and another along the outer edge V_o. If the V_o direction is suppressed, then the V_c direction will dominate the electrodeposition process, leading to the formation of NCAs.[12–14]

Currently, available nanoimprinting techniques include nanothermal imprinting, ultraviolet (UV) curing imprinting, and micro-contact printing. Among these techniques,[15–19] UV curing imprinting is widely adopted in the precision printing industry due to its advantages of rapid curing, energy efficiency, environmental friendliness, and high processing precision. Using acrylic resin for UV curing imprinting can be a good choice for enhancing the successful rate of transfer. During the UV curing process, the photo-initiator triggers polymerization instantaneously. Besides, the properties of the resin itself can determine the optical film's refractive index and hydrophobicity. These properties are essential for achieving desired performance characteristics in optical films.[20]

Herein, we report a novel strategy using electrodeposited NCAs as a templates for fabricating 3A optical films in a simple, scalable and general manner. The obtained 3A optical film exhibits a water droplet contact angle greater than 90°, demonstrating excellent hydrophobic properties, with a reflectivity of approximately 4%, transmittance of 89.29%, and haze of 30.42%, showcasing excellent 3A optical performance. This research represents a significant breakthrough in applying nanotechnology to engineer advanced optical films.

Results and discussion

Through nanotechnology involving electrochemical control of screw dislocation growth, we regulated the crystal's growth direction to fabricate a template with NCA (Fig. 1a–d). The step edges created by screw dislocations provide low-energy barriers, making them suitable sites for the adsorption of ions or complexes. Nickel ions primarily deposit at the step edges of the screw dislocations (Fig. 1a and b). The crystal growth driven by spiral dislocations can occur in two directions: the direction of the dislocation core (V_c) and the outer edge direction (V_o) (Fig. 1c). When a crystal growth inhibitor is added to the electroplating solution, it limits the growth in the V_o direction, thereby promoting growth in the V_c direction. In the presence of ammonium chloride, nickel ions exist in the form of nickel-ammonium complexes ($[Ni(NH_3)_6]^{2+}$), which have high separation energy. With the increase of separation energy, more activation energy is required for nickel layer growth, leading to suppressed growth in the V_o direction and allowing V_c to dominate the electrodeposition process, facilitating the
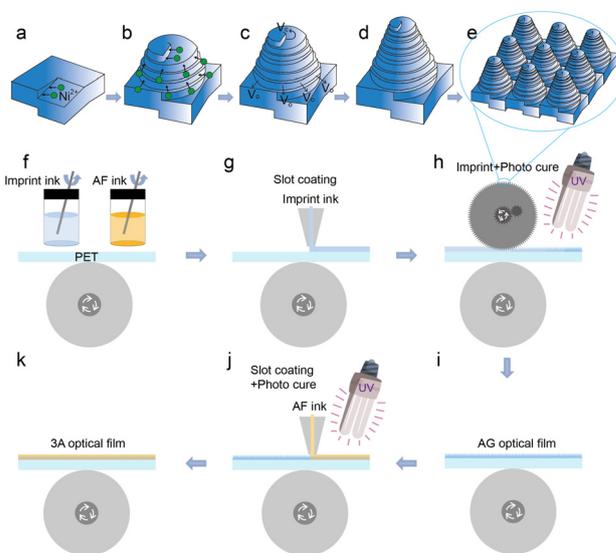
Fig. 1 (a–e) Screw dislocation growth mechanism of NCAs; (f–k) preparation process of the 3A optical film. (f) Preparation of imprint ink; (g) slit coating of imprint ink onto the substrate; (h) imprinting and UV curing of the imprint ink on the substrate; (i) demoulding to obtain AGF; (j) slit coating UV curing of AF; (k) as-obtained 3A optical film.

formation of NCAs (Fig. 1d and e). The process for preparing 3A optical films *via* nanoimprinting generally includes several steps: formulating the resin ink to enable AG property, slit coating the resin ink, imprinting and UV curing, demoulding to achieve the AG layer, and coating AF ink (Fig. 1f–k). Herein, NCAs are used as a template to uniformly transfer patterns onto the resin ink coating on optically clear polymer surfaces, such as polyethylene terephthalate (PET) films (Fig. 1f and g). The resin ink on the PET surface is cured by applying a UV light on the other side of the substrate (Fig. 1h), resulting in an AG optical film with a pitted micro–nano structure (noted as AGF), as shown in Fig. 1i. Finally, a thin layer of AF ink is coated onto the surface of the sample and subjected to UV curing to ultimately obtain a 3A optical film (Fig. 1j and k).

The parameters of the electrodeposition process are critical to the surface morphology of the NCA templates, particularly for achieving a large area of uniform nanostructures. Firstly, we investigated the effect of electrodeposition time on nickel deposition and characterized the samples using optical microscopy (Fig. S1†). The results from optical microscopy indicate that the sample with a 5 mins deposition time has a partially deposited surface (Fig. S1a†) which exhibits a light color; while those samples with a deposition time of 10 min or more exhibit a dark color (Fig. S1b†), indicating different coating thicknesses. Elongating the deposition time to 20 min results in uneven and rough surfaces (Fig. S1d†). In contrast, the samples deposited for 10 min and 15 min were relatively uniform (Fig. S1b and c†). To assess the morphology of the coatings at different electrodeposition times, we further performed scanning electron microscopy (SEM) characterization (Fig. 2a–d). The SEM images demonstrate the influence of deposition time on morphology. The morphology of the sample deposited for 5 min is conical but still in its formative stage, covering only a partial area (Fig. 2a). In comparison, the sample deposited for 20 min shows large cones, with some areas exhibiting flower-like growths (Fig. 2d), which is undesirable. When comparing the samples deposited for 10 min and 15 min (Fig. 2b and c), the 10 min sample displays a more

ordered conical structure and a more consistent morphology that aligns better with our requirements. Therefore, we consider the morphology of the sample deposited for 10 min to be optimal, making it suitable for subsequent experiments.

Besides deposition time, deposition temperature is another important influencing factor. The electrodeposition temperature affects the deposition speed and the uniformity of the coating, which is crucial for obtaining high-quality electrodeposition products. As the deposition temperature increases, the NCA thickness typically increases because higher temperatures facilitate the deposition reaction rate, allowing for its rapid growth. Elevated electrodeposition temperatures help accelerate electroplating kinetics, leading to the formation of additional dislocation structures. Additionally, higher temperatures can improve the conductivity of the deposition solution, promote anodize dissolution, reduce pinhole defects, and lower internal stress within the deposited layer.[21] However, excessively high temperatures may also cause excessive convection in the plating solution, leading to insufficient edge over-plating. To further identify the influence of reaction temperature, here we conducted relative experiments and characterized the samples using optical microscopy (Fig. S2†). The results from optical microscopy indicate that the sample deposited at a temperature of 55 °C has a partially deposited surface (Fig. S2a†); while those samples at a temperature of 60 °C exhibit no defect areas (Fig. S2b†), indicating a uniform outlook. Raising the deposition temperature to 65 °C and 70 °C resulted in a partially deposited surface (Fig. S2c and d†). The optical microscopy images indicate that 60 °C is the optimal condition for electrodeposition. To assess the morphology of the coatings at different electrodeposition temperatures, we further performed scanning SEM characterization (Fig. 2e–h). The SEM images clearly illustrate the influence of electrodeposition temperature on morphology. The electrodeposition cones are tiny and exhibit flower-like growths at an elevated temperature of 70 °C (Fig. 2h), which is undesirable. The flakes are insufficiently developed with some flower-like morphology at the temperature of 65 °C (Fig. 2g), rendering them unsuitable for transfer print. The cone grew incompletely at the temperature of 55 °C (Fig. 2e). In contrast, the sample deposited at 60 °C were relatively uniform (Fig. 2f), meeting the requirements for transfer imprint. Therefore, we consider that the morphology of the sample deposited at 60 °C is optimal, where the samples can be used in subsequent experiments.

In addition to electrodeposition time and temperature, another important influencing factor is current density. It is a critical parameter in the deposition process, directly affecting the reaction rate and deposition speed.[22] Generally, higher current densities can accelerate the electrochemical reaction rate, leading to an increased deposition speed. However, if the current density is too high, it can result in a decline in coating quality, causing burning, higher roughness, bubbling, *etc*. Moreover, different deposited metals and various deposition processes have different requirements for current density. The deposition rate of some metal materials is very sensitive to
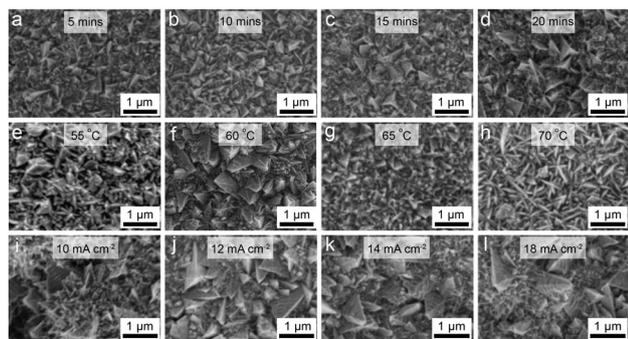
Fig. 2 SEM images of samples prepared under different deposition parameters. (a–d) Varying time (5 min, 10 min, 15 min and 20 min); (e–h) different temperatures (55 °C, 60 °C, 65 °C and 70 °C); (i–l) various current densities (10 mA cm^{-2}, 12 mA cm^{-2}, 14 mA cm^{-2} and 18 mA cm^{-2}).

current density, while others are less sensitive. Therefore, it is essential to select an appropriate current density based on actual conditions during the electrodeposition process to achieve optimal deposition results.[23]

To observe the deposition morphology under different current densities, we conducted optical microscopic characterization (Fig. S3†). The images reveal distinct differences in the coatings at varying current densities. At a current density of 10 mA cm^{-2}, the partial outlooks of the copper foil substrate remained the same (Fig. S3a†), indicating that the current density was too low. In contrast, at 18 mA cm^{-2}, the sample exhibited uneven deposition with localized defects (Fig. S3d†). Under optical microscopy, there were no significant differences in the sample morphology at current densities of 12 mA cm^{-2} and 14 mA cm^{-2} (Fig. S3b and c†), suggesting that further SEM characterization is necessary.

SEM images of the samples (Fig. 2i–m) reveal the morphological differences at different current densities. Conical structures were observe at the current density of 10 mA cm^{-2} d. However, most of the conical structures were incomplete (Fig. 2i). Well-defined NCA structures with uniform morphology were observed at the current densities of 12 mA cm^{-2} and 14 mA cm^{-2} (Fig. 2j and k). Shattered structures appeared in neighbouring NCAs when the current density was increased to 18 mA cm^{-2} (Fig. 2l), which is undesirable. Based on these observations, we can conclude that the optimal conditions were achieved at current densities of 12 mA cm^{-2} and 14 mA cm^{-2}. Considering the overall impact of current density on electrodeposition, relatively lower current densities lead to a more uniform electrodeposition layer. Therefore, we consider the optimal electrodeposition current density to be 12 mA cm^{-2}.

The above experimental results indicate that the desired outcome is a uniform coating with a conical nanostructure. Through controlling reaction parameters, we determined the optimal conditions include: a current density of 12 mA cm^{-2}, an electrodeposition temperature of 60 °C, and an electrodeposition time of 10 min. Subsequent electrodeposition will be carried out under these conditions.

To achieve an effective transfer of patterns after obtaining the NCA templates, the substrate must possess good transparency so that it can transmit UV light for curing the resin during the UV curing process, allowing the acrylate-based imprint resin ink to quickly cure. Additionally, the cured resin should have good adhesion to the substrate surface while weak adhesion to the NCA template ensured better demoulding capability.

There are many resins with high refractive index and optical clarity on the market, which are praised for having a weak adhesion to metal and a strong adhesion to the substrate. For this purpose, we screened out four common UV-curable resins for study. To optimize the performance of the optical films, we investigated the properties of L-6907 release UV resin and Z-975-H03C acrylic resin. The L-6907 release UV resin did not peel off after curing and exhibited strong adhesion to metal substrates (Fig. S4a and b†). In contrast,

while the Z-975-H03C acrylic resin could be peeled off after transfer, a significant amount of resin remained on the metal substrate, making complete demoulding difficult (Fig. S4c and d†). Considering the strong adhesion of the two resins between the NCA template and the substrate, neither L-6907 release UV resin nor Z-975-H03C acrylic resin was suitable. Consequently, we explored two fluorinated resins: 1240 fluorocarbon-modified UV resin and 2150 fluorosilicone-modified UV resin. The experimental results showed that these two resin inks exhibited significantly better adhesion on PET substrates compared to their adhesion on NCAs, demonstrating excellent transfer and peeling performance (Fig. S4e–h†). Further characterization of their micro-morphology was conducted using SEM (Fig. S5†). It was observed that some conical structures failed to transfer from the fluorocarbon resin surface (Fig. S5a†), likely due to residual resin remaining on the microstructure template and not fully peeled off. In contrast, the SEM characterization results for the fluorosilicone resin were more favorable, with almost all conical morphologies successfully transferred and no residual resin observed on the template (Fig. S5b†). Based on the SEM observations, we prioritized this fluorosilicone resin as the main component of the transfer ink.

As for the substrate film, we selected five commercially available optical film substrates with significant market shares, which are C8fr, Shinkong Co. (PET, 125 μm), U483, Toray Co. (PET, 125 μm), PU-H403, Longhua Co. (Polymethyl Methacrylate, PMMA, 60 μm), P960RR, TacBright Optronics Co.(Triacetyl Cellulose, TAC film, 60 μm), and TA044, Toyobo Co. (Super Re-orientation Film, SPF, 80 μm). They all exhibit excellent optical clarity but show different natures or surface finishing layers. A comparative study was conducted on these different substrates to evaluate the transfer effectiveness.

Based on the transfer results, we determined that when using PET C8fr as the substrate, the fluorosilicone resin ink was effectively cured after exposure to UV light, allowing for smooth demoulding of the samples (Fig. S6a†). Accordingly, C8fr was selected as the substrate for pattern transfer. In contrast, although the resin ink was also cured under UV exposure when using U483 as substrate, its adhesion was poor, and the cured optical film could not be smoothly demoulded from the NCA template (Fig. S6b†). Additionally, the other three substrates—PU-H403, P960RR, and TA044—seem to block too much of the UV curing light (Fig. S6c–e†), as even after multiple UV curing steps with maximized irradiation energy, the same ink still failed to cure. Through the above tests, we decided to choose C8fr as the substrate for better transfer.

Fig. 3a shows the NCA template obtained through electrodeposition as the transfer substrate. SEM images of the template show that the NCAs are uniformly distributed on the template (Fig. 3b and c). During the transfer process, the resin is applied to the substrate, forming microstructures on the optical film through structural transfer. The optical film exhibits bright outlook photographic images (Fig. 3d), indicating a high level of haze. SEM observation further reveals that the surface of the optical film has micro–nano pit structures
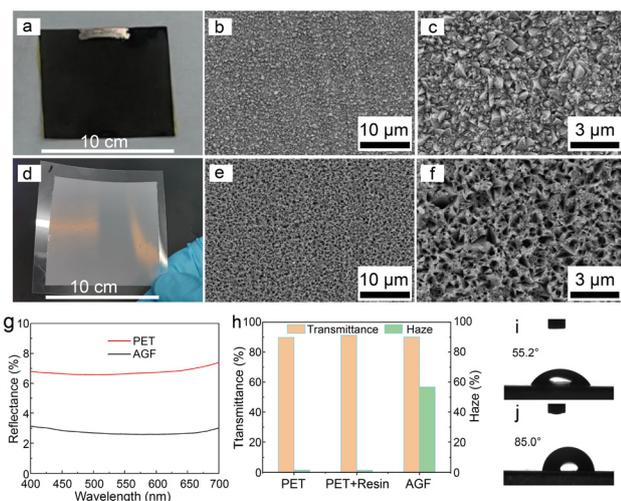
Fig. 3 (a) Photographic image and (b and c) SEM images of the NCAs template. (d) Photographic image and (e and f) SEM images of the AGF (g) reflectance spectrum of the C8fr (PET) substrate and the AGF. (h) Transmittance and haze of the PET substrate and the AGF. Contact angle measurements of (i) the PET substrate and (j) the AGF.

corresponding to those on the template (Fig. 3e and f), confirming that the microstructures have been successfully transferred onto the optical film, which causes surface refraction and higher optical haze.

Measurement of the reflectivity of the PET substrate before and after transfer print within the wavelength range of 400 nm to 700 nm showed that the reflectivity of the bare PET substrate was approximately 7%, while the reflectivity after transferring the optical film decreased to about 3% (Fig. 3g). This change indicates that AGF effectively alters its surface refractive index characteristic, causing interference of the incident light between the film layers and thereby reducing reflective losses. The significantly reduced reflectivity demonstrates that the resulting optical film possesses excellent anti-reflective properties, successfully reducing the glare problem.

When observing the contact angle changes by adding water droplets to the surface of the C8fr substrate and the transferred optical film, the results showed no significant change in contact angle after pattern transfer. Specifically, the contact angle of the PET substrate was 55.2° (Fig. 3i), while the contact angle of AGF was 85.0° (Fig. 3j). Although the contact angle of AGF increased relative to that of the PET substrate, indicating improved hydrophobicity, it remained below 90°. This suggests that the bare PET substrate doesn't intrinsically show AF performance.

To observe the AF performance of the samples, we monitored the changes in contact angle by adding water droplets to the PET surface coated with the commercial F26C AF resin, Taier Co. The measured contact angle for the PET substrate was 54.5°, while the contact angle of AGF after coating the AF resin increased to 102.4° (Fig. S7†). This indicates that the contact angle significantly increased after applying the AF resin, which suggests that the applied coating exhibits good

hydrophobic properties. Further testing of the anti-reflective performance of the AF resin film itself showed that the reflectivity of the PET optical film was approximately 7%, whereas the reflectivity of the AF resin-coated PET was about 6% (Fig. S8†). This indicates that the AF resin did not significantly reduce reflectivity. We also measured the transmittance, haze, and color coordinates of the samples coated with AF resin (Table S1†). Compared to the bare PET substrate, there was a slight increase in transmittance after applying the AF resin, while the changes in color coordinates were insignificant. Due to the lack of microstructure in the AF resin itself, its haze value was relatively low. These results demonstrate that the AF resin endows hydrophobicity to the substrate, while a flat AF resin coating layer alone cannot provide AG functionality, as can be expected. To achieve 3A effect, AG can be realized simultaneously by introducing microstructures, AF can be realized by introducing AF resin, and AR can be realized by constructing interfaces with different gradient refractive indices. However, achieving 3A performance in a simple fabricating process is very challenging.

To achieve optical films with 3A performance, we combined the nano-imprinted optical film with AF resin. We coated the AF resin onto the surface of AGF and observed the surface morphology of AGF samples coated with 1%, 2%, 3%, 4%, and 5% AF resin concentrations, corresponding to the dry film of 50 nm, 100 nm, 150 nm, 200 nm, and 250 nm using SEM (Fig. 4a–f). AGF itself exhibited micro–nano structures corresponding to the morphology on the template (Fig. 4a). As the thickness of AF resin applied to the optical film surface increased, the thickness of the AF resin left on the surface after drying and curing also gradually increased, filling in the micro–nano structures imprinted on the optical film surface. Consequently, the surface of the optical film became increasingly smoother, and the microscopic features obtained through structural transfer began to disappear (Fig. 4b–f). At the AF resin thicknesses of 50 nm and 100 nm, distinct micro–nano structures were still visible (Fig. 4b and c), but when the thickness reached 150 nm, these structures significantly diminished (Fig. 4d). At the thicknesses of 200 nm and 250 nm, the micro–nano structures on the optical film's surface completely disappeared (Fig. 4e and f). We also measured the water droplet contact angles on the optical films coated with different thicknesses (0 nm, 50 nm, 100 nm, 150 nm, 200 nm, and 250 nm) of AF resin (Fig. S9a–f†). The results showed that the contact angle for the uncoated optical film was 85.0°, while it increased to 85.6° after coating with 50 nm AF resin (Fig. S9a and b†), both being less than 90°, indicating no significant hydrophobic effect. As the thickness of AF resin increased, the contact angles for thicknesses of 100 nm, 150 nm, 200 nm, and 250 nm were measured at 86.2°, 99.0°, 99.9°, and 101.3°, respectively (Fig. S9c–f†). A noticeable transition from hydrophilicity to hydrophobicity occurred between the AF resin thicknesses of 100 nm and 150 nm (Fig. 4g). When the thicknesses exceeded 150 nm, the optical film exhibited good hydrophobic properties. This study highlights that optimizing AF resin thickness is crucial for enhan-
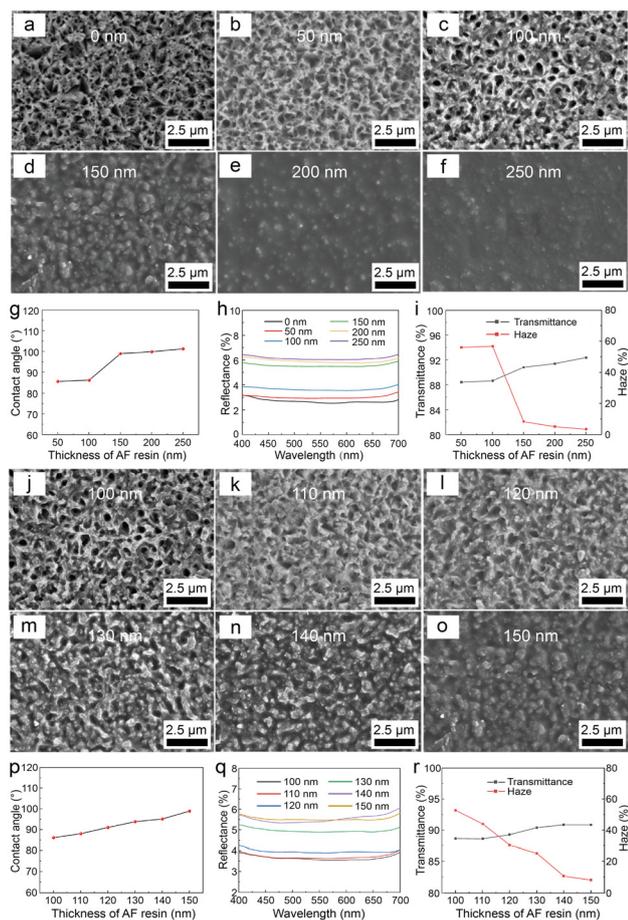
Fig. 4 SEM characterization and performance analysis of optical films with different thickness of AF resin: (a–f) surface morphology evolution with increasing thickness (0 nm, 50 nm, 100 nm, 150 nm, 200 nm and 250 nm); (g) contact angle measurements of films with coatings thickness from 50 nm to 250 nm; (h) reflectivity spectra of films with coatings thickness from 0 nm to 250 nm; (i) optical properties (total transmittance and haze) variation with coating thickness; (j–o) surface morphology evolution with increasing thickness (100 nm, 110 nm, 120 nm, 130 nm, 140 nm and 150 nm); (p) contact angle measurements of films with coatings thickness from 100 nm to 150 nm; (q) reflectivity spectra of films with coatings thickness from 100 nm to 150 nm; (r) optical properties (total transmittance and haze) variation with coating thickness.

cing both AF performance and maintaining desirable optical characteristics in AGF. For a thicker over-coated resin layer, it fails to adequately infiltrate the underlying pits. The heights of the nanocones are approximately 1 micron, which facilitates the partial filling of the dried resin layer in the pits. This configuration helps maintain a certain level of AG property and is beneficial for sustaining a specific gradient in refractive index differences, thereby achieving a reduction in reflectance.

As the dried film thickness of the AF resin increases, the contact angle of the optical film gradually rises, enhancing its hydrophobic properties and approaching the hydrophobic characteristics of the AF resin itself. This finding indicates that by adjusting the thickness of AF resin, the hydrophobic performance of the optical film can be effectively improved, pro-

viding a better solution for practical applications. When measuring the reflectivity of optical films coated with different thicknesses of AF resin, the results showed that as the thickness increased, the reflectivity gradually rose, with the reflectivity curve shifting upwards. The reflectivity of both the uncoated optical film and those coated with 50 nm and 100 nm AF resin remained below 4% in the wavelength range of 400–700 nm, indicating good anti-reflective (AR) performance. However, when the thickness of AF resin reached 150 nm or higher, a significant increase in reflectivity was observed, suggesting a loss of AR performance (Fig. 4h). With increasing thickness of AF resin, the thickness of the film formed on the optical film surface after curing also increased. Once the film thickness reached a certain value, the micro–nano structures on the optical film surface gradually disappeared, leading to changes in both transmittance and haze. Further measurements were conducted on transmittance, haze, and color coordinates for optical films without AF resin and those coated with 50 nm, 100 nm, 150 nm, 200 nm, and 250 nm thicknesses of AF resin (Table S2†). The results indicated that as the thickness of AF resin increased, the overall transmittance of the optical film improved while haze decreased. Additionally, there was a decrease in the *b* value of color coordinates, suggesting an increase in yellowing effects. A notable transition in transmittance, haze, and color coordinates occurred between the AF resin thicknesses of 100 nm and 150 nm (Fig. 4i). In summary, by adjusting the thickness of AF resin, not only can the hydrophobic performance of the optical film be enhanced, but its optical properties can also be optimized, leading to superior performance in practical applications.

Through the measurement of the effects of different thicknesses (from 50 nm to 250 nm) of AF resin on the performance of optical films, it was found that the AF, AR, and AG properties of the coated optical films underwent significant changes within the thickness range of 100 nm–150 nm. Therefore, the optimal thickness of AF resin is determined to be between 100 nm and 150 nm. To further identify the best condition for 3A performance, we continued to refine the thickness gradient within this range, testing thicknesses of 110 nm, 120 nm, 130 nm, 140 nm, and 150 nm of AF resin. When observing the surface morphology of the AGF samples coated with different thicknesses (100 nm, 110 nm, 120 nm, 130 nm, 140 nm, 150 nm) of AF resin using SEM, it was noted that as the thickness of AF resin increased, the surface of AGF gradually became smoother, with the original micro–nano structures progressively disappearing (Fig. 4j–o). Specifically, AGF retained some micro–nano structures at AF resin thicknesses from 100 nm to 130 nm, (Fig. 4j–m). However, when the thickness reached 140 nm and 150 nm, these micro–nano pits were almost completely filled by AF resin and significantly diminished (Fig. 4n and o). Contact angle measurements for optical films coated with different thicknesses of AF resin revealed that the contact angles for coatings with 100 nm and 110 nm AF resin were 86.2° and 88.1°, respectively (Fig. S10a and b†), both being less than 90°, indicating poor hydrophobic

performance. In contrast, contact angles for coatings with thicknesses of 120 nm, 130 nm, 140 nm, and 150 nm were measured at 91.1°, 93.9°, 95.2°, and 99° (Fig. S10c–f†). A transition from hydrophilicity to hydrophobicity occurred around an AF resin thickness of approximately 120 nm (Fig. 4p), with contact angles exceeding 90° for coatings with thicknesses greater than this threshold. As the thickness of AF resin increased from 100 nm to 150 nm, the AF performance of the optical film gradually approached that of the AF resin itself, resulting in an increase in contact angle and enhanced hydrophobicity. Reflectivity measurements for optical films coated with different thicknesses of AF resin indicated that reflectivity gradually increased with rising thicknesses (Fig. 4q). Specifically, when coated with AF resin thicknesses between 100 nm and 120 nm, reflectivity remained below approximately 200 nm, indicating good AR performance; however, when the thickness exceeded 130 nm, reflectivity increased significantly, indicating a loss of AR performance. The optical film transferred onto a PET substrate effectively adjusted the refractive indices across different layers due to its micro–nano structure, resulting in interference effects that reduced reflective losses. However, as the thickness of AF resin increased, these micro–nano pits gradually disappeared, leading to a decline in antireflective performance and an increase in reflectivity. When measuring total transmittance, color coordinates, and haze changes for optical films coated with varying thicknesses of AF resin between 100 nm and 150 nm, results showed that haze decreased while total transmittance exhibited an increasing trend (Fig. 4r), primarily due to the gradual disappearance of micro–nano pits on the surface of the optical film. Additionally, a decrease in the b value of color coordinates indicated an improvement in yellowing effects (Table S3†). Through comparative analysis of the performance under different thicknesses of the AF resin regarding their combined AG, AR, and AF performances it was determined that an optimal coating thickness of AF resin is around 120 nm. Under these parameters, we observed the topographical features on the surface of the 3A optical film by oblique SEM and AFM. The pits with a diameter of approximately 500 nm on the optical film's surface correspond to the nanomorphology of the nanocone array (Fig. S11a, b, d and e†). The surface roughness (R_a) of the 3A optical film and the nanocone array is 72.3 and 120.0 nm, respectively (Fig. S11c and e†). This undulating morphology reduces the proportion of light reflection while altering the angle of transmitted light upon striking the optical film's surface, resulting in refraction and enhanced haze. We compared the anti-reflection, anti-glare, and anti-fingerprint effects of the obtained 3A optical film with PET (Fig. S12†), verifying the superior 3A performance of our final product. This selection will aid in achieving high-performance optical films that exhibit excellent AG, AR, and AF performances simultaneously.

To realize AG property, conventional methods utilize the refractive index differences between microparticles and resin to induce greater diffuse reflection by printing such a mixture on the optical film surface. As for AR films, conventional strategies are to reduce the refractive index difference between air and the coated material to lower reflectance, traditionally accomplished through magnetron sputtering multiple layers with gradient refractions. To achieve AF properties, coating a layer of amphiphobic material (particularly, hydrophobic one) is a general strategy, which has previously been realized through chemical vapor deposition (CVD) methods. Simultaneously meeting the three functionalities—AG, AR, and AF—poses a significant challenge that requires a combination of various complex processes. However, we have demonstrated that it is possible to achieve the three functionalities using only slit coating and nanoimprinting techniques, representing an innovative breakthrough in the field of 3A optics. By comparing our results with commercially available 3A films (GFT6E03-P33) (Table S5†), we find that while performance remains comparable, our simpler nanoimprinting technology allows for the production of 3A optical films in a much simpler and cost-effective way. As an original study in the application of nanoimprinting technology for 3A film production, there remains substantial room for performance enhancement. Our research highlights the significant potential of nanoimprinting technology in the fabrication of 3A films.

Conclusions

In summary, we demonstrated the control over crystal dislocation growth through nanotechnology to obtain templates with NCAs, which can work as superwetting nanoelectrodes for renewable energy collection on nanoscale. Utilizing these templates, we employed nano-imprinting and UV-curable resin techniques to fabricate optical films with porous micro–nano structures on PET surfaces, achieving excellent 3A performance. We investigated the effects of different electrodeposition times, temperatures, and current densities on the morphology of NCAs, ultimately determining the optimal experimental conditions for electrodeposition: a current density of 12 mA cm^{-2}, a deposition temperature of 60 °C, and a deposition time of 10 min. These conditions resulted in templates that exhibited excellent AG performance upon transfer. Furthermore, we explored the impact of different resin types and their thicknesses on the contact angle and reflectivity of the optical films. As the thickness of AF resin increased, both the contact angle and reflectivity gradually increased. At an AF resin thickness of approximately 120 nm, a transition from hydrophilicity to hydrophobicity occurred, with contact angles exceeding 90°, indicating good hydrophobicity. At this thickness, the reflectivity was about 4%, transmittance was 89.29%, and the haze was 30.42%. Ultimately, we obtained optical films characterized by high haze, low reflectivity, high transmittance, and excellent hydrophobic properties, demonstrating outstanding 3A performance. This work illustrates the significant potential applications of nano-imprinting technology in the field of 3A optical film fabrication.

Author contributions

K. Gan designed the experiment and processed the experimental data. K. Gan and S. Li carried out the experiments. K. Gan wrote the manuscript. H. Zhu, W. Pan, and R. Yao revised the manuscript. C. Yang revised the manuscript and supervised the work.

Data availability

The data supporting this article have been included as part of the ESI.†

Conflicts of interest

The authors declare no conflict of interest.

Acknowledgements

References

1 G. Li, M. C. Tseng, Y. Chen, F. S. Yeung, H. He, Y. Cheng, J. Cai, E. Chen and H. S. Kwok, *Light: Sci. Appl.*, 2024, **13**, 301.

2 W. Li, Y. Chen and Z. Jiao, *Nanomaterials*, 2023, **13**, 1570.

3 C. Wang, Y. Fan, J. Sun and J. Shao, *Opt. Mater.*, 2023, **145**, 114385.

4 K. Chansomwong, Y. H. Kim, H. Lee and B.-S. Bae, *J. Sol-Gel Sci. Technol.*, 2020, **95**, 447–455.

5 D. Tulli, S. D. Hart, P. Mazumder, A. Carrilero, L. Tian, K. W. Koch, R. Yongsunthon, G. A. Piech and V. Pruneri, *ACS Appl. Mater. Interfaces*, 2014, **6**, 11198–11203.

6 L. Chen, H. Liang, P. Liu, Z. Shu, Q. Wang, X. Dong, J. Xie, B. Feng and H. Duan, *ACS Nano*, 2024, **18**, 23968–23978.

7 Z. Huang and Y. Lin, *Nanoscale*, 2022, **14**, 16749–16760.

8 Y. Chen, Z. Shu, Z. Feng, L. A. Kong, Y. Liu and H. Duan, *Adv. Funct. Mater.*, 2020, **30**, 2002549.

9 M. Onodera, M. Ataka, Y. Zhang, R. Moriya, K. Watanabe, T. Taniguchi, H. Toshiyoshi and T. Machida, *ACS Appl. Mater. Interfaces*, 2024, **16**, 62481–62488.

10 Z. Su, C. Yang, B. Xie, Z. Lin, Z. Zhang, J. Liu, B. Li, F. Kang and C. P. Wong, *Energy Environ. Sci.*, 2014, **7**, 2652–2659.

11 Z. Lei, P. Liu, X. Yang, P. Zou, A. Nairan, S. Jiao, R. Cao, W. Wang, F. Kang and C. Yang, *Small*, 2023, **19**, e2301247.

12 L. Peng, H. Zhu, H. Wang, Z. Guo, Q. Wu, C. Yang and H.-Y. Hu, *Nat. Commun.*, 2023, **14**, 5734.

13 P. Liu, B. Chen, C. Liang, W. Yao, Y. Cui, S. Hu, P. Zou, H. Zhang, H. J. Fan and C. Yang, *Adv. Mater.*, 2021, **33**, 2007377.

14 A. Nairan, C. Liang, S.-W. Chiang, Y. Wu, P. Zou, U. Khan, W. Liu, F. Kang, S. Guo, J. Wu and C. Yang, *Energy Environ. Sci.*, 2021, **14**, 1594–1601.

15 C. Raksiri, P. Potejanasak and T. Dokyor, *Polymers*, 2023, **15**, 3804.

16 I. Shahine, Q. Hatte, M. Harnois and P.-Y. Tessier, *ACS Appl. Electron. Mater.*, 2024, **6**, 2281–2288.

17 C. Shi, J. Jiang, C. Li, C. Chen, W. Jian and J. Song, *Nat. Commun.*, 2024, **15**, 8839.

18 D. Su, W. L. Wu, P. Q. Sun, Y. C. Yuan, Z. X. Chen, Y. F. Zhu, K. Y. Bi, H. L. Zhou and T. Zhang, *Adv. Sci.*, 2024, **11**, e2305469.

19 M. Xue, F. Li and T. Cao, *Nanoscale*, 2012, **4**, 1939–1947.

20 Y.-M. Ha, E. Cho, H. T. Lim, J. C. Won, Y. H. Kim, Y. S. Kim and J. Kim, *Mater. Today Commun.*, 2022, **33**, 104370.

21 L. Zheng and X. Peng, *Met. Mater. Int.*, 2018, **24**, 1293–1302.

22 Z. Chen, C. Zhu, M. Cai, X. Yi and J. Li, *Appl. Surf. Sci.*, 2020, **508**, 145291.

23 S. K. Padamata and G. Saevarsdottir, *Front. Chem.*, 2023, **11**, 1133990.